

# Effect of oxygen nonstoichiometry on electrotransport and low-field magnetotransport property of polycrystalline $\text{La}_{0.5}\text{Sr}_{0.5}\text{MnO}_{3-\delta}$ thin films

J.-M. Liu\*

*Laboratory of Solid State Microstructures, Nanjing University, Nanjing 210093, People's Republic of China and Institute of Materials Research and Engineering, 3 Research Link, Singapore 117602*

Q. Huang, J. Li, and C. K. Ong

*Department of Physics, National University of Singapore, Singapore 119260*

Z. C. Wu, Z. G. Liu, and Y. W. Du

*Laboratory of Solid State Microstructures, Nanjing University, Nanjing 210093, People's Republic of China*

(Received 4 November 1999; revised manuscript received 21 March 2000)

Polycrystalline  $\text{La}_{0.5}\text{Sr}_{0.5}\text{MnO}_{3-\delta}$  thin films deposited on quartz wafers at 680 °C and various oxygen pressures  $P$  by pulsed laser deposition are prepared. The effects of oxygen nonstoichiometry on the microstructural, electrotransport and low-field magnetotransport property of the thin films are investigated in details. A structural distortion from the stoichiometric lattice is identified for the samples deposited at  $P < 0.1$  mbar. It is verified that the thin-film conductivity over the Curie point follows variable-range hopping. The carrier density at the Fermi surface falls and the metal-insulating transition shifts toward low temperature with decreasing  $P$ , with a jump at  $P = 0.1$  mbar. Enhanced low-field magnetoresistance at low temperature is achieved for  $P > 0.1$  mbar. Oxygen overdeficiency at  $P \leq 0.1$  mbar essentially prohibits the spin reordering. The temperature dependence of the electro- and magnetotransport properties is explained by the two-channel model where the insulating channels and metallic ones coexist in parallel.

## I. INTRODUCTION

The discovery of colossal magnetoresistance (CMR) in doped rare-earth manganese perovskite oxides and others has stimulated intensive research activities.<sup>1,2</sup> A high magnetoresistance ratio MR ( $\text{MR} = [\rho(0) - \rho(H)]/\rho(0)$ , where  $\rho$  is the sample resistivity and  $H$  is the applied magnetic field) under high magnetic field has been reported for a number of doped rare-earth manganese oxides. At the same time, several physical approaches to the CMR phenomenon have been proposed.<sup>1,3-7</sup>

The stoichiometric  $\text{La}_{1-x}\text{Ca}_x\text{MnO}_3$  (LCMO) or  $\text{La}_{1-x}\text{Sr}_x\text{MnO}_3$  (LSMO) shows a ferromagnetic transition at temperature  $T = T_c$ , where the MR ratio reaches the maximal.<sup>6</sup> At the same time an insulator-metal transition appears at  $T = T_m \sim T_c$  due to the so-called double-exchange (DE) mechanism.<sup>3</sup> As  $T > T_c$ , the conduction follows either the variable-range hopping (VRH) mechanism<sup>8</sup> for polycrystalline samples or small polaron hopping (SPH) one<sup>9,10</sup> for epitaxial or single-crystal samples.<sup>11,12</sup>  $T_m$  in polycrystalline LSMO or LCMO is much lower than that in single crystal, whereas its low-field MR ratio (LFMR) at low  $T$  is much higher than that in single crystals.<sup>2,13,14</sup> This excess contribution is believed to mainly originate from spin-polarized tunneling (SPT) or spin-dependent scattering (SDS) associated with grain boundaries (GBs).<sup>13</sup> On the one hand, the double-exchange mechanism is currently used to explain the electrotransport behavior of single-crystal LCMO or LSMO for which the simultaneous hopping of an electron from the  $\text{Mn}^{3+}$  site to the central oxygen ion and the other from the oxygen ion to the  $\text{Mn}^{4+}$  site is responsible. Here oxygen

vacancies are essential for the ferromagnetism and electron hopping. On the other hand,  $\text{MR} \propto (M/M_s)^2$  is satisfied before the magnetic saturation reached for polycrystalline LCMO or LSMO, where  $M$  is the magnetization of the system and  $M_s$  is the saturated  $M$ .<sup>15</sup> As  $H$  is raised over the saturated field, the MR response becomes linear against  $H$ , controlled by the spin-disordered layers available, such as GBs.<sup>16,17</sup> Therefore, the generation of a number of spin-disordered sites in the microstructure can be an essential scheme to enhance LFMR.

Nevertheless, LFMR enhancement in these oxides remains a big challenge to us.<sup>18</sup> The embedding of spin-disordered ranges in the microstructure is emphasized, including grain size refining and grain boundary generation,<sup>17-21</sup> porous microstructure fabrication,<sup>22</sup> surface crack processing,<sup>23</sup> and metal-insulator mixed sintering,<sup>24,25</sup> in addition to the lanthanide or alkaline-earth doping<sup>26,27</sup> and boundary deoxidization<sup>28</sup> as well. In this article we explore the effect of oxygen deficiency on the electro- and magnetotransport properties and thus LFMR in polycrystalline LSMO ( $x=0.5$ ) thin films. A direct argument is that oxygen vacancies (OV) frozen in LSMO may change a lot the hopping conduction and hinder the double exchange,<sup>29,30</sup> thus producing number of localized spin-disordered ranges. A correspondence between the density of OVs and LFMR may be available.

## II. EXPERIMENTAL DETAILS

The LSMO thin films of variable oxygen concentration were prepared on quartz wafers at adjusted pressure  $P$  of oxygen ambient by means of pulsed laser deposition (PLD).

Quartz substrates were chosen for several reasons here. The first is to avoid the potential effect of crystalline substrates on the film orientation. Second, the density of OV's in the films can be enhanced in the polycrystalline sample rather than the epitaxial sample. In fact, our previous work revealed that a modulation of density of OV's over a wide range in epitaxial LSMO is not easy, even if  $P$  was reduced to  $10^{-6}$  mbar. However, this becomes much easier in polycrystalline LSMO thin films,<sup>28,29</sup> since GBs in polycrystalline LSMO can be seriously oxygen deficient at low  $P$ . Finally, the stress effect commonly available in epitaxial growth can be minimized if amorphous wafers are used here.

The PLD experiment was performed by using a KrF excimer laser of 248 nm in wavelength and 30 ns in pulse width. An optimized laser fluency of  $1.6 \text{ J/cm}^2$  and replate of 5 Hz were utilized and the substrate temperature  $T_s$  of  $680^\circ\text{C}$  was kept during the ablation. A dense ceramic LSMO disk was chosen as target. The detailed PLD procedure was described earlier.<sup>29</sup> The pressure  $P$  of the flowing oxygen in the chamber was precisely adjustable from  $10^{-6}$  to 2 mbar. Films of 800 nm in thickness and  $10 \times 1.0 \text{ mm}^2$  in in-plane dimension were deposited and then cooled down to room temperature at the same  $P$ . The film thickness was measured by atomic force microscopy (AFM) and confirmed with cross-section profiling.

The microstructure of the films was checked by fine step-mode x-ray diffraction (XRD). The grain size was evaluated with AFM. The Oxford superconducting vibrating sample magnetometer (VSM) was used to characterize the magnetic property of the samples. The electro- and magnetotransport properties were measured by using the standard four-pad probe with the sample temperature well controlled. A triangle-wave ac magnetic field of  $\pm 4 \text{ kOe}$  in magnitude and 0.01 Hz in frequency was applied in parallel to the sample surface.

### III. EXPERIMENTAL RESULTS AND DISCUSSION

#### A. Microstructural evaluation

The XRD  $\theta$ - $2\theta$  spectrum for a series of samples deposited at different  $P$  is presented in Fig. 1. All films are polycrystalline, and (110), (111), (200), (211), and (220) reflections are identified. Starting from  $P=0.5 \text{ mbar}$  until  $P=0.14 \text{ mbar}$ , the positions of the XRD peaks show no identifiable difference from those of the target. However, the target is (110) favored, but the films prefer (111). The film lattice parameters remain the same as the target.

At  $P=0.1 \text{ mbar}$ , a very strong (200) peak is recorded, whereas (111) and (211) reflections almost vanish. However, the peak positions show no identified change. Subsequently, as  $P=60 \mu\text{bar}$  and lower, a distinct shift of (111), (200), and (211) peaks toward the low-angle direction is found, as indicated by arrows, while the (110) peak remains stationary. A lattice distortion is probed. The spacing expansion along [111] and [211] is 1.7% and 2.5%, respectively, and 2.2% for [200]. The (200) peak decays sharply down to a comparable level to others and almost vanishes as  $P \leq 10 \mu\text{bar}$ . Since the (110) peak remains unmoved, one may not be able to give details of the lattice distortion just from the  $\theta$ - $2\theta$  scan. Nevertheless, the distortion takes place once  $P \leq 0.1 \text{ mbar}$ . It is

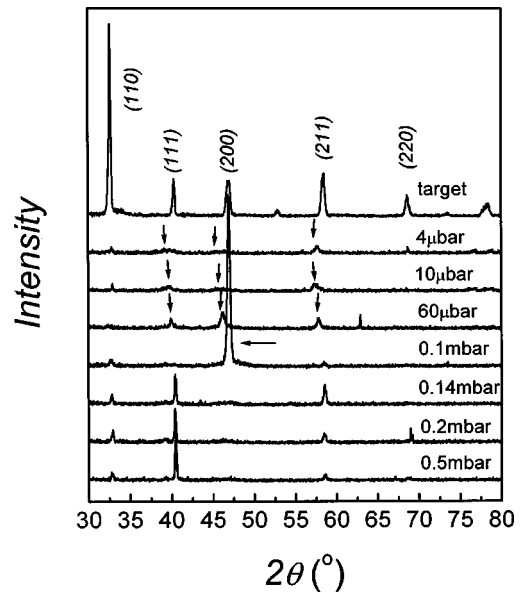


FIG. 1. XRD spectra for a series of LSMO thin films deposited at different values of  $P$  as indicated. The spectrum for the LSMO target is inserted for reference.

small, but imposes a significant influence on the electro- and magnetotransport of the films.

The lattice distortion may be ascribed to several particulars in the samples, such as fluctuations of GBs, cation stoichiometry, or strain against the change of ambient pressure  $P$ . The AFM observation of grain size for these films does not expose a remarkable change. Coarser grains of  $\sim 100 \text{ nm}$  for the films deposited at  $P > 0.1 \text{ mbar}$  are imaged, but the average grain size for the films for  $P = 4 \mu\text{bar}$  is  $\sim 80 \text{ nm}$ . No remarkable grain refining can be identified. The contribution to sample conductivity due to change of the GB *volume fraction* is small, taking a note that the GBs contribute to the sample resistivity.

In order to discard the possible cation nonstoichiometry due to the change of  $P$ , the chemical constitution of the film deposited at  $P = 10 \mu\text{bar}$  was checked by transmission electron microscopy (TEM, Philips CM-300) equipped with an energy-dispersive x-ray (EDX) spectrometer. The data show that the relative atomic ratio La:Sr:Mn roughly meets the stoichiometry within the measuring uncertainty, indicating that no cation deficiency or accumulation appears in the films prepared at low  $P$ . In fact, it is believed that evaporation of heavy elements like La, Sr, and Mn during laser ablation is not sensitive to the variation of the oxygen pressure. And more, as we mentioned earlier, the effect of stress in the films can be forgotten too since the films are  $\sim 800 \text{ nm}$  thick and deposited on quartz substrates. The thin strained layer, if any, neighboring the substrate surface just contributes a negligible part to the shift of XRD probed peaks. Therefore, variation of the oxygen vacancy density depending on the oxygen pressure remains the only factor responsible for the fluctuations of the microstructure and transport property.

#### B. Electro- and magnetotransport property

A tremendous dependence of the zero-field electrical resistivity  $\rho_0$  and magnetic moment  $M$  on  $P$  is shown. The

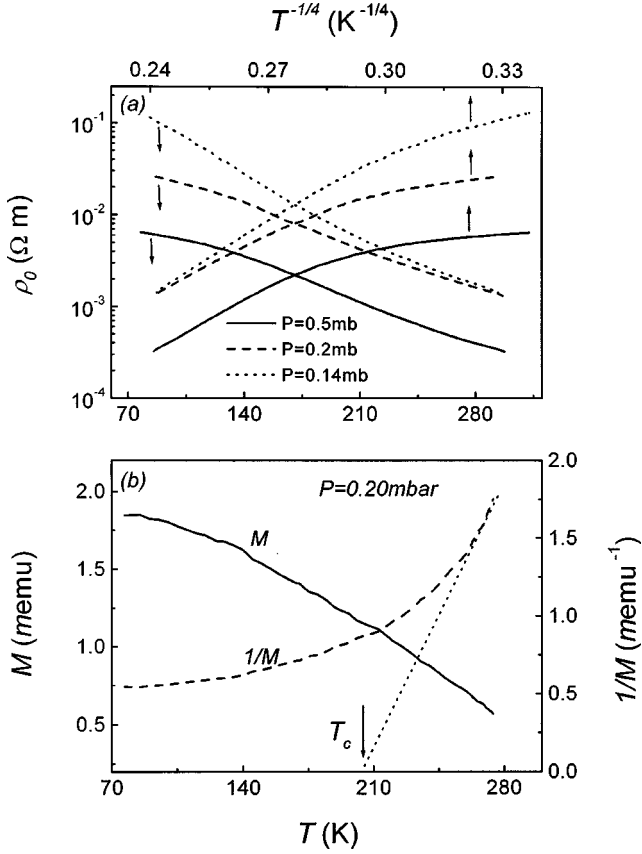


FIG. 2. (a) Zero-field resistivity  $\rho_0$  as a function of  $T$  and  $T^{-1/4}$  for three LSMO thin films deposited at 0.5, 0.2, and 0.14 mbar and (b) magnetic moment  $M$  and its reciprocal  $1/M$  as a function of  $T$  for LSMO thin film deposited at 0.2 mbar.

measured  $\rho_0 \sim T$  relation favors the insulating-type conduction for all samples. Figure 2(a) presents the data for three samples at  $P > 0.1$  mbar. The  $\ln \rho_0 \sim T$  relation is roughly linear at high  $T$ , but nonlinear at low  $T$ . The occurrence of an insulator-metal transition is clearly indicated by the sublinearization. Nevertheless, no distinct resistivity peak is observable unless  $T < 77$  K, the lowest temperature available to us because of existence of GBs.  $T_m$  for the samples can be given by an indirect definition.

While the conduction at  $T < T_c$  (or  $T_m$ ) follows the metal-like behavior, it has been established that the polycrystalline LSMO over  $T_m$  exhibits the VRH conduction:<sup>31</sup>

$$\rho_0 = \rho_{i0} \exp(T_0/T)^{1/4}, \quad (1)$$

where  $\rho_{i0}$  is the prefactor and  $T_0$  the characteristic temperature. The conduction at high  $T$  far over  $T_m$  may operate in terms of the SPH mechanism:<sup>12</sup>

$$\rho_0/T = \rho_{p0} \exp(E_p/kT), \quad (2)$$

where  $\rho_{p0}$  is the prefactor,  $E_p$  represents the activation energy for small polaron, and  $k$  is the Boltzmann constant. The SPH conduction commonly works well for over-room-temperature data. Really, a fitting of the data on the three samples does not support the SPH unless  $T$  is close to room temperature ( $> 280$  K), while the VRH mechanism works quite well for all data. As shown in Fig. 2(a), a plot of  $\ln \rho_0$  against  $T^{1/4}$  produces good linearity once  $T$  is higher than a

TABLE I. Fitted data of  $T_0$ ,  $T_c$ ,  $N(E_F)$ , and  $E_p$  for LSMO thin films deposited at different  $P$ .

$P$ (mbar)	$T_0$ (MK)	$T_m$ (K)	$N(E_F)$ (eV m) <sup>-3</sup>	$E_p$ (meV)
0.50	9.853	201	$1.1884 \times 10^{26}$	97.84
0.20	12.272	188	$9.5418 \times 10^{25}$	98.44
0.14	16.080	172	$7.2819 \times 10^{25}$	100.18
0.10	111.615	<77	$1.0491 \times 10^{25}$	104.63
0.06	161.177	<77	$7.2650 \times 10^{24}$	112.38
0.01	170.335	<77	$6.8744 \times 10^{24}$	132.67
0.004	176.860	<77	$6.6207 \times 10^{24}$	134.71

critical value, which is defined as  $T_m$ . The as-defined  $T_m$  is really very close to  $T_c$  as evaluated from the VSM data. The measured moment  $M$ , and  $1/M$  as well, as a function of  $T$  for the sample prepared at  $P = 0.2$  mbar is presented in Fig. 2(b).  $T_c \sim 200$  K, very close to  $T_m \sim 188$  K, is derived from Fig. 2(a). The values of  $T_m$  for the three samples are given in Table I, from which one sees a downshift of  $T_m$  with decreasing  $P$ .

As  $P \leq 0.1$  mbar, the as-prepared samples show no more magnetization over  $T > 77$  K, indicating  $T_c < 77$  K. The measured  $\rho_0 \sim T$  relationships are plotted in Fig. 3, from which a big change is observed, referring to the two curves at  $P$

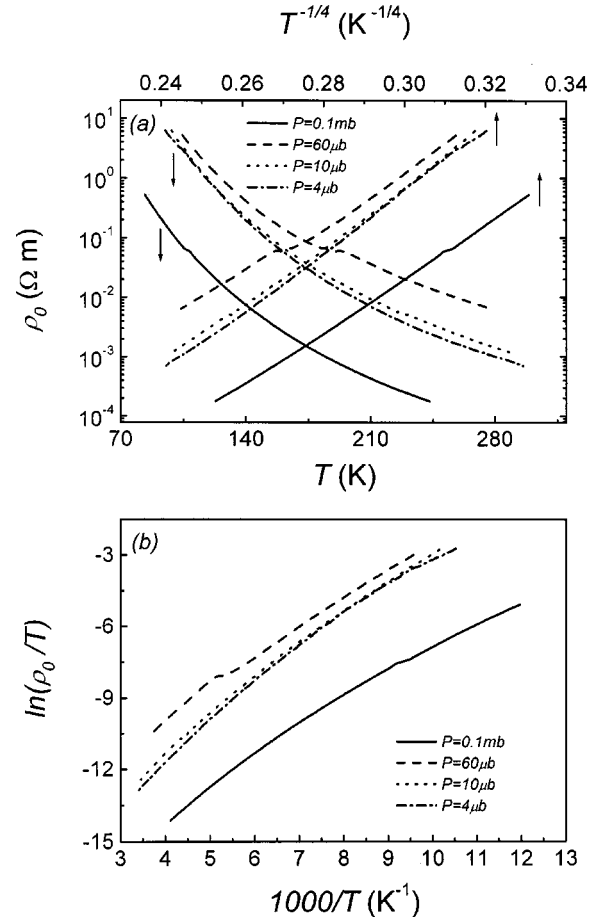


FIG. 3. (a) Zero-field resistivity  $\rho_0$  as a function of  $T$  and  $T^{-1/4}$  for four LSMO thin films deposited at 0.1 mbar, 60  $\mu$ bar, 10  $\mu$ bar, and 4  $\mu$ bar, respectively, and (b)  $\ln(\rho_0/T) \sim 1/T$  relations for the four samples.

$=0.14$  and  $0.1$  mbar, respectively. Note that the lattice distortion occurred at  $P \leq 0.1$  mbar. It is clearly shown that the conduction follows VRH in a much better manner than SPH. A perfect linear  $\ln \rho \sim T^{1/4}$  relationship is demonstrated for all samples [Fig. 3(a)], while no sample fits well the  $\ln(\rho_0/T) \sim T$  relationship [Fig. 3(b)]. When  $T_0$  for the three samples at  $P > 0.1$  mbar is  $\sim 10^7$  K, a big jump up to  $10^8$  K is extracted for the samples deposited at  $P \leq 0.1$  mbar. The fitted values of  $T_0$  are listed in Table I, from which the carrier density at the Fermi surface,  $N(E_F)$ , is estimated via<sup>31</sup>

$$N(E_F) = \frac{24}{\pi \xi^3 k T_0}, \quad (3)$$

where  $\xi$  is the localization length for LSMO, i.e., Mn-Mn separation. Taking  $\xi = 0.39$  nm, one obtains  $N(E_F)$  for all samples, as shown in Table I. Noting  $N(E_F) = 10^{28} - 10^{29} \text{ eV}^{-1} \text{ m}^{-3}$  for stoichiometric LSMO single crystals,<sup>32</sup> the as-prepared thin films have a much lower  $N(E_F)$ , which falls down with decreasing  $P$ . If the conduction bandwidth for LSMO remains unchanged at  $1.5 \text{ eV}$ ,<sup>33</sup> the real hole carrier density, which is of the same order of magnitude as  $N(E_F)$ , decreases with decreasing  $P$ . This provides us direct evidence that more oxygen vacancies are frozen in the lattice when the thin film is deposited at a lower value of  $P$ . The density will be so high once  $P \leq 0.1$  mbar that a lattice distortion appears. A similar phenomenon was reported earlier for  $\text{La}_{0.5}\text{Sr}_{0.5}\text{CoO}_3$  thin films.<sup>34</sup>

On the other hand, the best fitted  $E_p$  for different samples are given in Table I just for a qualitative discussion, supposing the SPH mechanism works too. The evaluated  $E_p$ , over  $90 \text{ meV}$  as  $P > 0.1$  mbar and even reaching  $112$  and  $134 \text{ meV}$  as  $P = 60$  and  $4 \mu\text{bar}$ , respectively, is consistent with the data reported earlier.<sup>12</sup> It is then suggested that the electron-lattice interaction would be greatly enhanced in oxygen-deficient thin films.

It is basically understandable that oxygen vacancies frozen in the samples hinder the localized electron hopping via the DE mechanism. Although the conduction bandwidth data and details of the lattice distortion are unavailable to us, as justified previously<sup>12</sup> and confirmed presently, the oxygen vacancies contribute extrinsically to the VRH conduction.

### C. Low-field magnetoresistance

The LFMR effect is strongly dependent on  $P$  as  $P > 0.1$  mbar, however, seriously damaged once  $P \leq 0.1$  mbar. It is reasonable to correlate this damage with high density of OVs in the samples. As an example, the resistivity  $\rho$ - $H$  loop at  $77 \text{ K}$  for the sample at  $P = 0.2$  mbar is shown in Fig. 4(a). The MR  $\sim H$  hysteresis (here  $\text{MR} = \rho/\rho_0 - 1$ ) for three samples is plotted in Fig. 4(b). First, the MR response to varying  $H$  shows typical MR- $H$  hysteresis. The peak location is the same as the magnetic coercivity  $H_c$ . Second, the MR response can be roughly classified into two parts. In part I where  $|H| \leq 800 \text{ Oe}$ , the response is seriously nonlinear and a sharp decreasing of  $\rho$  is observable once  $H$  deviates from  $H_c$ . The resistivity reduction at low field (lower than the field for reaching  $M_s$ ) is attributed to the movement of the ferromagnetic domain walls and spin alignment inside the domains if any and at the walls, i.e.,<sup>13-15</sup>

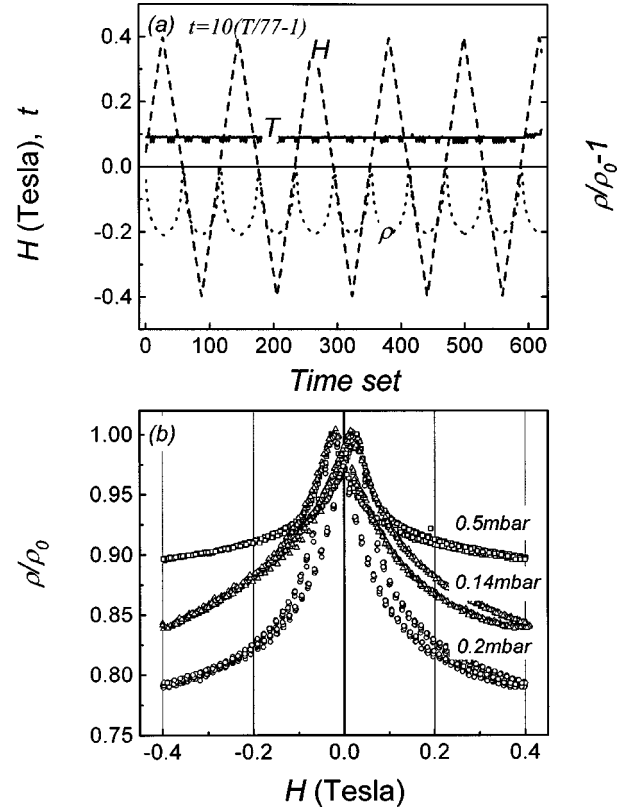


FIG. 4. (a) Measured MR ratio ( $\rho/\rho_0 - 1$ ) for a LSMO thin film deposited at  $P = 0.2$  mbar together with recorded  $H$  and  $T$  as a function of time set and (b) measured MR  $\sim H$  hysteresis loops measured at  $T = 77 \text{ K}$  for three LSMO thin films at  $P = 0.5, 0.2,$  and  $0.14$  mbar, respectively.

$$\text{MR} = \Delta\rho/\rho(0) \propto (M/M_s)^2, \quad (4)$$

which is independent of structural defects such as GBs and OVs. A direct verification of Eq. (4) is given in Fig. 5 where the MR  $\sim H$  loop and  $M \sim H$  loop for the sample at  $P = 0.2$  mbar are plotted. Equation (4) is roughly satisfied as long as  $H \leq 800 \text{ Oe}$ . For part II where  $|H| > 2000 \text{ Oe}$ , the field dependence of MR becomes roughly linear and the path correlation of the response is no longer remarkable. This is

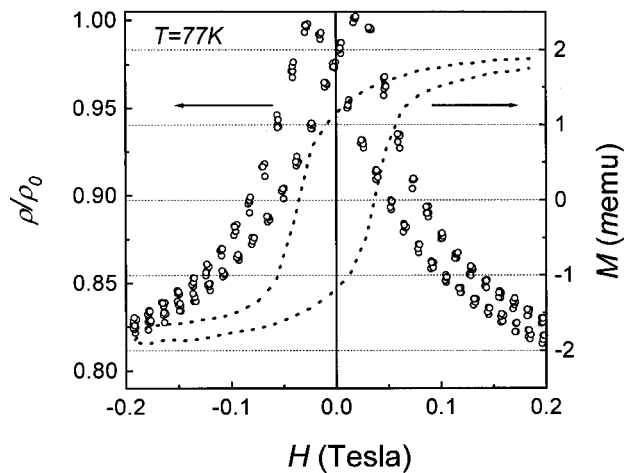


FIG. 5. Measured MR  $\sim H$  and  $M \sim H$  hysteresis at  $T = 77 \text{ K}$  for a LSMO thin film prepared at  $P = 0.2$  mbar.

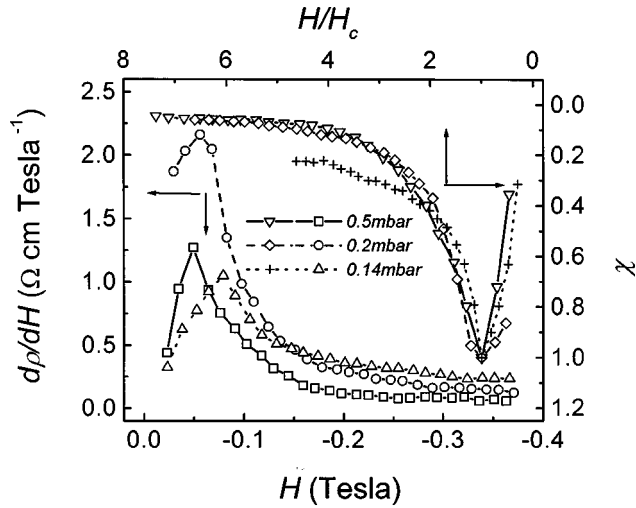


FIG. 6.  $d\rho/dH \sim H$  and  $\chi \sim H/H_c$  relations at  $T=77$  K for three LSMO thin films deposited at  $P=0.5, 0.2,$  and  $0.14$  mbar.

attributed to the spin-disordered ranges centered at GBs and OV. Since the grain size for the three samples remains similar, OVs represent the main source for the difference in the MR response.

As  $P=0.5$  mbar, the MR effect in part II is very weak so that an almost horizontal line is obtained. The sample at  $P=0.2$  mbar shows the maximal LFM, up to 21% at  $H=\pm 4$  kOe. The field for prohibiting the path correlation is the lowest at  $P=0.5$  mbar and highest at  $P=0.14$  mbar. A higher field predicts more spin-disordered sites in the sample. To get insight into the role of OVs, we plot  $d\rho/dH$  against  $H$  and  $\chi=(d\rho/dH)/(d\rho/dH)_{H=H_c}$  against  $H/H_c$  in Fig. 6. Note here that  $\rho=\rho_0$  at  $H=H_c$ . A good coincidence of the three  $\chi \sim H/H_c$  curves over  $H/H_c=1-2.5$  confirms once more that Eq. (4) is satisfied no matter with how much the oxygen vacancy density in the sample is. The coercivity  $H_c$  is slightly enhanced with decreasing  $P$ , confirmed by a shift of the  $d\rho/dH$  peak toward high field. This is also an indication of the appearance of more spin-disordered sites. The same argument applies when noting that on the right of  $(d\rho/dH)_{H=H_c}$ ,  $d\rho/dH$  takes the highest at  $P=0.14$  mbar and the lowest at  $P=0.5$  mbar. If this tendency is retained, a higher MR ratio is expected at a much higher field for the sample deposited at lower  $P$ . Once  $P \leq 0.1$  mbar, the samples show no more ferromagnetic moment at  $T > 77$  K, and LFM at 77 K falls down to a few percent ( $\sim 4\%$ ), as presented in Fig. 7.

From all of the results presented above, it can be concluded that oxygen vacancies as induced by low-pressure deposition produce a number of spin-disordered sites at low  $T$ . These disordered sites can be reordered at a higher field so that part II of the MR response can be enhanced. However, overoptimized OVs weaken ferromagnetism and damage the electrotransport property. Especially, as  $P \leq 0.1$  mbar, the induced high-density OVs result in lattice distortion and prohibit the ferromagnetic state at all. The LFM and high-field MR are intrinsically prohibited.

#### D. Two-channel model

The oxygen-vacancy-induced spin-disordered sites may form insulating chainlike clusters that distribute randomly,

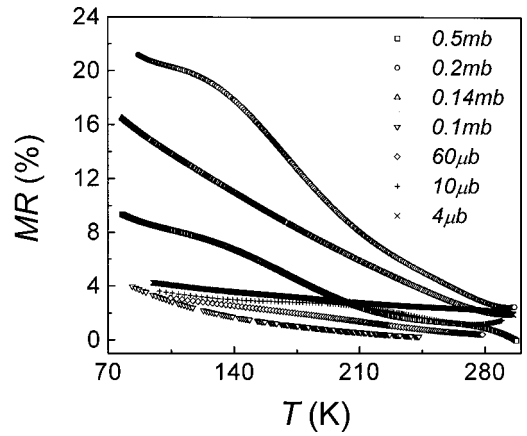


FIG. 7. MR ratio at  $H=4$  kOe as a function of  $T$  for a series of LSMO thin films prepared at different values of  $P$  as indicated.

but uniformly, in the microstructure and coexist with the other ranges that are metallic like. When the density of OVs increases up to some value, percolating spin-disordered networks may form in the microstructure. Such a configuration can be described by the two-channel model proposed by Andres *et al.*<sup>20</sup> We give here a modified physical picture for this model. Two types of conduction channels, insulating conduction channels (ICCs) and metallic conduction channels (MCCs), are supposed to align in parallel. From the authors' opinion, the interfacial layers between the two types of channels remain spin disordered at zero field or very low field. Part of these spin-disordered interfacial layers may be reordered at a field enough low, but much higher than,  $H_c$ . In addition, GBs can be viewed as a mixing of the two types of channels. Those GBs with intimately contacted grains may be metallic ones and other GBs with heavy OVs are thought to be insulating, as proposed in the original model.<sup>20</sup>

The conduction for the ICCs and MCCs follows, respectively,

$$\begin{aligned} \rho_i &= \rho_{i0} \exp(T_0/T)^{1/4}, \\ \rho_m &= a + bT, \end{aligned} \quad (5)$$

where  $\rho_i$  remains the same as Eq. (1) and  $\rho_m$  is the resistivity for MCCs,  $a$  and  $b$  are constants to be determined. The total resistivity  $\rho$  is then written as

$$\rho = (\rho_i^{-1} + g\rho_m^{-1})^{-1}, \quad (6)$$

where  $g$  represents the geometrical parameter, which depends not only the applied field, but also the two-channel configuration. Substituting Eq. (5) into Eq. (6), one obtains

$$\rho = \left\{ \frac{1}{\rho_{i0} \exp(T_0/T)^{1/4}} + \frac{g/a}{1 + (b/a)T} \right\}^{-1}. \quad (7)$$

Equation (7) is used to fit our data at zero field and  $H=4$  kOe in order to evaluate four parameters  $\rho_{i0}$ ,  $T_0$ ,  $g/a$ , and  $b/a$ . Because ICCs make little contribution to the MR effect, Fig. 8(a) just presents the fitted  $g/a$  and  $b/a$ , whereas  $T_0$  at zero field is given in Table I. It is revealed that  $\rho_{i0}$  decreases rapidly, but  $T_0$  is raised with decreasing  $P$ . They shift slightly up and down, respectively, once the field is applied.

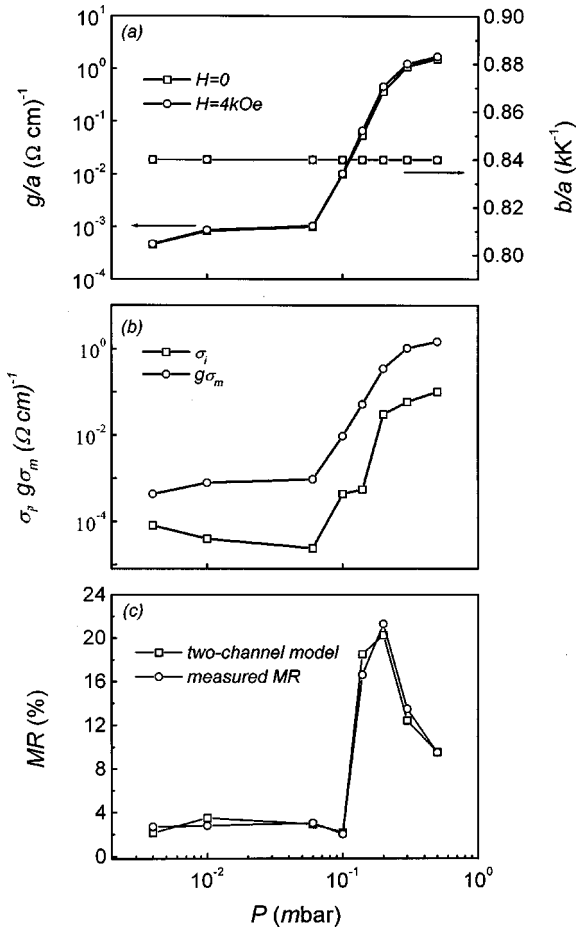


FIG. 8. (a) Evaluated parameters  $g/a$  and  $b/a$  at zero field and  $H=4 \text{ kOe}$ , (b) evaluated  $\sigma_i$  and  $g\sigma_m$ , and (c) measured and two-channel model predicted MR ratio at  $T=77 \text{ K}$  as a function of  $P$ .

The fitting shows that the parameter  $b/a$  remains unchanged around  $8.4 \times 10^{-4} \text{ K}^{-1}$ , no matter what the field or  $P$  is. This is reasonable, noting that once one oxygen vacancy is frozen at some site, the local electron hopping is hindered so that MCCs no longer apply to this site. The parameter  $g/a$  both at zero field and  $H=4 \text{ kOe}$ , however, falls rapidly over three orders of magnitude as  $P$  decreases from 0.5 to 0.06 mbar and then remains stable for further descending  $P$ . A slight upshift of  $g/a$  is observed as  $H > 0$ , which reflects the change of magnetotransport under the applied field.

Equation (6) can be rewritten in terms of conductivity:

$$\sigma = \sigma_i + g \cdot \sigma_m, \quad (8)$$

where  $\sigma = 1/\rho$ , and  $\sigma_i$  and  $\sigma_m$  are the conductivity for ICCs and MCCs. Since  $\sigma_i$  does not change much against  $H$  and we always have  $\sigma_i \ll g\sigma_m$  at low temperature as shown in Fig. 8(b), the MR ratio can be written as

$$\text{MR} \cong \frac{\Delta\sigma_m}{\sigma_m(H)} + \frac{\Delta(g/a)}{(g/a)(H)}, \quad (9)$$

where  $\sigma_m(0) \sim \sigma_m(H)$  is taken since  $\Delta\sigma \ll \sigma$  ( $\Delta\sigma/\sigma < 2 \sim 3\%$  at 77 K and 4 kOe for epitaxial LSMO).<sup>13,15</sup>

The first term on the right side of Eq. (9) takes accounts of the MR ratio at very low field ( $H \sim H_c$ ), i.e., Eq. (4), independent of  $g/a$ . The second term is mainly the contribution at  $H \gg H_c$  and much higher than that required for  $M = M_s$ . Noting that  $\Delta\sigma_m/\sigma_m \ll \Delta(g/a)/(g/a)$ , Eq. (9) can be simplified as

$$\text{MR} \approx \frac{\Delta(g/a)}{(g/a)(H)}. \quad (10)$$

A plotting of the measured MR ratio at 77 K and calculated MR ratio via Eq. (10) at  $H=4 \text{ kOe}$  yields a good coincidence between them, as shown in Fig. 8(c). The model predicts a serious damage of the MR effect once  $P \leq 0.1$  mbar, whereas enhanced LFMR is acquired at an optimized pressure of  $P=0.20$  mbar. Taking into consideration several approximations, the two-channel model seems to be a quite reasonable description of the electro- and magnetotransport phenomena in oxygen-deficient LSMO polycrystalline thin films.

#### IV. CONCLUSION

In conclusion, we have investigated the microstructure and electro- and magnetotransport properties of oxygen-deficient LSMO polycrystalline thin films deposited at reduced pressures of oxygen, by pulsed laser deposition. A significant influence of oxygen nonstoichiometry on these properties has been demonstrated. The lattice distortion from the pseudocubic perovskite for the thin films deposited at  $P \leq 0.1$  mbar has been identified from the fine XRD checking, and contributes to the electron-hopping prohibition. The as-deposited thin films show typical VRH conduction over the metal-insulating point. The carrier density at the Fermi surface is found to fall down about three orders of magnitude as the oxygen pressure decreases from 0.5 mbar to 4  $\mu\text{bar}$ . An enhanced 77 K LFMR of 21% at  $H=4 \text{ kOe}$  is demonstrated for the film deposited at  $P=0.2$  mbar. A higher density of oxygen vacancies, however, results in serious damage of LFMR down to 2–3%. The two-channel model where insulating channels and metallic ones coexist is used to explain the electro- and magnetotransport. A good consistency between the measured and calculated LFMR is presented.

#### ACKNOWLEDGMENTS

The authors would like to acknowledge financial support from the National Natural Science Foundation of China through special and normal projects, the National Key Project for Basic Research, and LSSMS of Nanjing University.

\*Email address: liujm@nju.edu.cn

<sup>1</sup>S. Jin, T. H. Tiefel, M. McCormack, R. A. Fastnacht, R. Ramesh,

and L. H. Chen, Science **264**, 413 (1994).

<sup>2</sup>C. N. R. Rao and B. Raveau, in *Colossal Magnetoresistance*,

- Charge Ordering and Related Properties of Manganese Oxides*, edited by C. N. R. Rao and B. Raveau (World Scientific, Singapore, 1998).
- <sup>3</sup>C. Zener, *Phys. Rev.* **82**, 403 (1951).
- <sup>4</sup>P. W. Anderson and H. Hasegawa, *Phys. Rev.* **100**, 675 (1955).
- <sup>5</sup>P. G. de Gennes, *Phys. Rev.* **118**, 141 (1960).
- <sup>6</sup>K. Chahara, T. Ohno, M. Kasai, and Y. Kozono, *Appl. Phys. Lett.* **63**, 1990 (1993).
- <sup>7</sup>P. Schiffer, A. P. Ramirez, W. Bao, and S. W. Cheong, *Phys. Rev. Lett.* **75**, 3336 (1995).
- <sup>8</sup>M. Viret, L. Ranno, and J. M. D. Coey, *Phys. Rev. B* **55**, 8067 (1997).
- <sup>9</sup>G. J. Snyder, R. Hiskes, S. DiCarolis, M. R. Beasley, and T. H. Geballe, *Phys. Rev. B* **53**, 14 434 (1996).
- <sup>10</sup>V. N. Krivoruchko and S. I. Khartsev, *Fiz. Nizk. Temp.* **24**, 1070 (1998) [*Low Temp. Phys.* **24**, 803 (1998)].
- <sup>11</sup>M. F. Hundley, M. Hawley, R. H. Heffner, Q. X. Jai, J. J. Neumeier, J. Tesmer, J. D. Thomson, and X. D. Wu, *Appl. Phys. Lett.* **67**, 860 (1995).
- <sup>12</sup>M. Ziese and C. Srinitiwarawong, *Phys. Rev. B* **58**, 11 519 (1998).
- <sup>13</sup>A. Gupta, G. Q. Gong, G. Xiao, P. R. Duncombe, P. Lecouer, P. Trouilloud, Y. Y. Wang, V. P. Dravid, and J. Z. Sun, *Phys. Rev. B* **54**, R15 629 (1996).
- <sup>14</sup>R. Mahesh, R. Mahendiran, A. K. Raychaudhuri, and C. N. R. Rao, *Appl. Phys. Lett.* **68**, 2291 (1996).
- <sup>15</sup>X. W. Li, A. Gupta, G. Xiao, and G. Q. Gong, *Appl. Phys. Lett.* **71**, 1124 (1997).
- <sup>16</sup>H. Y. Hwang, S. W. Cheong, N. P. Ong, and B. Batlogg, *Phys. Rev. Lett.* **77**, 2041 (1996).
- <sup>17</sup>B. Martinez, L. Balcells, J. Fontcuberta, and X. Obradors, *J. Appl. Phys.* **83**, 7058 (1998).
- <sup>18</sup>A. Gupta, in *Colossal Magnetoresistance, Charge Ordering and Related Properties of Manganese Oxides* (Ref. 2).
- <sup>19</sup>S. Lee, H. Y. Hwang, B. I. Shraiman, W. D. Ratchiff, and S. W. Cheong, *Phys. Rev. Lett.* **82**, 4508 (1999).
- <sup>20</sup>A. de Andres, M. Garcia-Hernandez, J. L. Martinez, and C. Prieto, *Appl. Phys. Lett.* **74**, 3884 (1999).
- <sup>21</sup>L. Balcells, J. Fontcuberta, B. Martinez, and X. Obradors, *Phys. Rev. B* **58**, R14 697 (1998).
- <sup>22</sup>X. L. Wang, S. X. Dou, H. K. Liu, M. Ionescu, and B. Zeimet, *Appl. Phys. Lett.* **73**, 396 (1998).
- <sup>23</sup>H. B. Peng, B. R. Zhao, Z. Xie, Y. Lin, B. Y. Zhu, Z. Hao, Y. M. Ni, H. J. Tao, X. L. Dong, and B. Xu, *Appl. Phys. Lett.* **74**, 1606 (1999).
- <sup>24</sup>L. Balcells, A. E. Carrillo, B. Martinez, and J. Fontcuberta, *Appl. Phys. Lett.* **74**, 4014 (1999).
- <sup>25</sup>D. K. Petrov, L. Krusin-Elbaum, J. Z. Sun, C. Field, and P. R. Duncombs, *Appl. Phys. Lett.* **75**, 995 (1999).
- <sup>26</sup>H. Y. Hwang, S.-W. Cheong, P. G. Radaelli, M. Marezio, and B. Batlogg, *Phys. Rev. Lett.* **75**, 914 (1995).
- <sup>27</sup>J. Fontcuberta, B. Martinez, A. Seffar, S. Pinol, J. L. Garcia-Munoz, and X. Obradors, *Phys. Rev. Lett.* **76**, 1122 (1996).
- <sup>28</sup>Q. Huang, C. K. Ong, J.-M. Liu, and J. Li (unpublished).
- <sup>29</sup>J. Li, J.-M. Liu, H. P. Li, H. C. Fang, and C. K. Ong, *J. Magn. Magn. Mater.* **202**, 285 (1999).
- <sup>30</sup>J. M. Liu and C. K. Ong, *Appl. Phys. Lett.* **73**, 1047 (1998).
- <sup>31</sup>N. Mott, *Conduction in Non-Crystalline Materials* (Clarendon, Oxford, 1993) p. 17ff.
- <sup>32</sup>B. F. Woodfield, M. L. Wilson, and J. M. Byers, *Phys. Rev. Lett.* **78**, 3201 (1997).
- <sup>33</sup>T. Saitoh, A. E. Bocquet, T. Mizokawa, H. Namatame, A. Fujimori, M. Abbate, Y. Takeda, and M. Takano, *Phys. Rev. B* **51**, 13 942 (1995).
- <sup>34</sup>J. M. Liu and C. K. Ong, *J. Appl. Phys.* **84**, 5560 (1998).